

Radiation hydrodynamics simulations of protoplanetary disks: Stellar mass dependence of the disk photoevaporation rate

AYANO KOMAKI,¹ RIOUHEI NAKATANI,² AND NAOKI YOSHIDA^{1,3,4}

¹*Department of Physics, The University of Tokyo, 7-3-1 Hongo, Bunkyo, Tokyo 113-0033, Japan*

²*RIKEN Cluster for Pioneering Research, 2-1 Hirosawa, Wako-shi, Saitama 351-0198, Japan*

³*Kavli Institute for the Physics and Mathematics of the Universe (WPI), UT Institute for Advanced Study, The University of Tokyo, Kashiwa, Chiba 277-8583, Japan*

⁴*Research Center for the Early Universe (RESCEU), School of Science, The University of Tokyo, 7-3-1 Hongo, Bunkyo, Tokyo 113-0033, Japan*

(Received; Revised; Accepted)

Submitted to ApJ

ABSTRACT

Recent multiwavelength observations suggest that inner parts of protoplanetary disks (PPDs) have shorter lifetimes for heavier host stars. Since PPDs around high-mass stars are irradiated by strong ultraviolet radiation, photoevaporation may provide an explanation for the observed trend. We perform radiation hydrodynamics simulations of photoevaporation of PPDs for a wide range of host star mass of $M_* = 0.5\text{--}7.0 M_\odot$. We derive disk mass-loss rate \dot{M} , which has strong stellar dependence as $\dot{M} \approx 7.30 \times 10^{-9} (M_*/M_\odot)^2 M_\odot \text{ yr}^{-1}$. The absolute value of \dot{M} scales with the adopted far-ultraviolet and X-ray luminosities. We derive the surface mass-loss rates and provide polynomial function fits to them. We also develop a semianalytic model that well reproduces the derived mass-loss rates. The estimated inner-disk lifetime decreases as the host star mass increases, in agreement with the observational trend. We thus argue that photoevaporation is a major physical mechanism for PPD dispersal for a wide range of the stellar mass and can account for the observed stellar mass dependence of the inner-disk lifetime.

1. INTRODUCTION

Recent infrared observations toward nearby star-forming regions revealed that the fractions of stars with circumstellar disks (protoplanetary disks; PPDs) decline with increasing the age of the star-forming region. The disk fraction as a function of age gives an approximate measure of the disk lifetime, and the results of the recent observations consistently suggest $t_{\text{life}} = 3\text{--}6 \text{ Myr}$ (e.g., Haisch et al. 2001; Meyer et al. 2007; Hernández et al. 2007; Mamajek 2009; Bayo et al. 2012; Ribas et al. 2014). Planets are formed from the gas and dust grains in PPDs, where dynamical interaction between planets and the parent disk shapes the initial configuration of the planetary system. The disk lifetime is thus an important factor in the study of planetary system formation.

There has been an intriguing suggestion from systematic infrared observations that the disk lifetime depends on the host star mass. Disks around massive stars have

shorter lifetimes than around low-mass stars (e.g., Carpenter et al. 2006; Lada et al. 2006; Allers et al. 2007; Dahm & Hillenbrand 2007; Kennedy & Kenyon 2009; Fang et al. 2012; Yasui et al. 2014; Ribas et al. 2015). Ribas et al. (2015) observe a number of associations and conclude that the disk lifetimes are systematically shorter for systems with a central star mass of $> 2 M_\odot$ than those with $< 2 M_\odot$. Similarly, Bayo et al. (2012) show that the disk fraction monotonically decreases as the mass of the central star increases in the range $0.1\text{--}1.7 M_\odot$. An apparently opposite trend has also been reported. Observations using Atacama Large Millimeter/submillimeter Array (ALMA) suggest that the *dust-disk* mass decreases systematically faster around lower-mass stars with $\sim 0.1\text{--}3 M_\odot$ (Ansdell et al. 2016; Pasucci et al. 2016; Ansdell et al. 2017). The physical mechanism that can account for these observations remains unknown.

Theoretical studies suggest three major disk-dispersal mechanisms: accretion (Shakura & Sunyaev 1973; Lynden-Bell & Pringle 1974), magnetohydrodynamic (MHD) winds (e.g., Suzuki & Inutsuka 2009; Turner

et al. 2014, for a review), and photoevaporation (e.g., Hollenbach et al. 1994; Shu et al. 1994; Alexander et al. 2014, for a review). Disk materials fall onto the host star by losing the angular momentum through viscous friction, while being stripped off from the disk surface by the winds. The disk dynamics and the mass evolution are determined by these effects mutually affecting each other (e.g., Clarke et al. 2001; Alexander et al. 2006; Owen et al. 2010; Wang et al. 2019; Gressel et al. 2020). The strengths of the effects and the dispersal timescale depend on the properties of the disk and the host star.

Photoevaporation is driven by the stellar far-ultraviolet (FUV; $6\text{ eV} \lesssim h\nu < 13.6\text{ eV}$), extreme-ultraviolet (EUV; $13.6\text{ eV} < h\nu \lesssim 100\text{ eV}$), and X-rays ($100\text{ eV} \lesssim h\nu \lesssim 10\text{ keV}$). Thermalizing electrons produced by photochemical reactions heat the disk gas, and the hot gas flows out of the disk and escapes from the gravitational potential of the central star. EUV photons are primarily absorbed by atomic hydrogen, while FUV and X-ray are absorbed also by dust grains and gas-phase metal species. FUV and X-ray photons can penetrate into deep interior regions of a disk with high column densities ($\sim 10^{21}\text{ cm}^{-2}$) (e.g., Richling & Yorke 2000; Ercolano et al. 2009; Gorti & Hollenbach 2009) and thus drive high-density photoevaporative flows. The rate of photoevaporation \dot{M} depends on the stellar UV and X-ray luminosities, and it is expected that \dot{M} increases with increasing stellar mass. In the light of this, the exact dependence of \dot{M} on the stellar mass can provide a clue to understanding the physical mechanism of disk dispersal and the observed trend of the disk lifetime.

In the present paper, we perform a set of radiation hydrodynamics simulations of disk photoevaporation. In order to examine the stellar mass dependence quantitatively, we systematically vary the host star mass and derive the disk photoevaporation rate when the system reaches a quasi-steady state. Gorti & Hollenbach (2009) explore the stellar mass dependence by studying the thermochemical structure of disks in hydrostatic equilibrium. They obtain \dot{M} for stars masses with $0.3\text{--}7.0\text{ M}_\odot$. Ideally, fully coupled radiation hydrodynamics simulations including thermochemistry are essential to derive the disk structure and the resulting \dot{M} self-consistently (Wang & Goodman 2017; Nakatani et al. 2018a,b). It is also important to follow the long-term evolution of photoevaporating disks (Nakatani et al. 2018a). We derive the stellar mass dependence, for the first time, by using multidimensional radiation hydrodynamics simulations.

The rest of the present paper is organized as follows. In Section 2, we explain the methods of our simulations. In Section 3, we show the result of our simulations. In

Section 4, we discuss the result. Finally, in section 5 we summarize.

2. NUMERICAL SIMULATIONS

We perform simulations of disk photoevaporation with varying the stellar mass in a wide range of $0.5\text{--}7.0\text{ M}_\odot$. The basic method is the same as Nakatani et al. (2018a,b). Briefly, we solve hydrodynamics, radiative transfer, and nonequilibrium chemistry in a fully coupled, self-consistent manner. Our simulations follow transfer of FUV, EUV, and X-ray radiation from the central star. The respective luminosities are adopted from Table 1 of Gorti & Hollenbach (2009) for stellar parameters of pre-main-sequence stars of age $\sim 1\text{ Myr}$ with $0.3\text{--}7\text{ M}_\odot$. The EUV and X-ray are assumed to originate from the chromosphere, while the FUV generated by accretion is additionally incorporated. The fiducial stellar parameters we use are shown in Table 1, where ϕ_{EUV} , L_{FUV} , and $L_{\text{X-ray}}$ are the emission rate of EUV photons, FUV luminosity, and X-ray luminosity, respectively. Since they are not well characterized by observations and can vary as the system evolves, we treat them as parameters and examine the overall effect on the disk mass-loss rate. In Section 3.4, we discuss the variability of photoevaporation rates by performing additional simulations with various luminosities for a few selected systems. We assume that the FUV radiation is contributed by continuum emission, and we do not explicitly take into account the hydrogen Ly α line, which has been suggested to be a substantial contributor to the total FUV flux in systems of classical T Tauri stars (Bergin et al. 2003; Herczeg et al. 2004; Schindhelm et al. 2012). In Section 3.4 we show the results of additional simulations with higher L_{FUV} . The simulations roughly correspond to the cases where the Ly α contribution is incorporated.

The disk gas contains eight chemical species; H I, H II, H_2 , H_2^+ , CO, O I, C II and electrons. We assume that C I is ionized to C II immediately after photodissociation of CO (Nelson & Langer 1997; Richling & Yorke 2000), so we do not include C I in the simulations. We set the dust-to-gas mass ratio to 0.01, the gas-phase elemental abundances of carbon to $y_{\text{C}} = 0.927 \times 10^{-4}$, and the gas-phase elemental abundance of oxygen to $y_{\text{O}} = 3.568 \times 10^{-4}$ (Pollack et al. 1994).

We assume an axisymmetric disk around the rotational axis and also assume symmetry with respect to the midplane. The simulations are performed in 2D spherical coordinates with all the three components

Table 1. Fiducial stellar parameters in the model (adopted from [Gorti & Hollenbach \(2009\)](#))

| M_* (M_\odot) | $\log \phi_{\text{EUV}}$ (/s) | $\log L_{\text{FUV}}$ (erg/s) | $\log L_{\text{X-ray}}$ (erg/s) |
|---------------------|-------------------------------|-------------------------------|---------------------------------|
| 0.5 | 40.1 | 30.9 | 29.8 |
| 0.7 | 40.5 | 31.3 | 30.2 |
| 1.0 | 40.7 | 31.7 | 30.4 |
| 1.7 | 41.0 | 32.3 | 30.7 |
| 3.0 | 39.0 | 32.9 | 28.7 |
| 7.0 | 44.1 | 36.5 | 30.8 |

of velocity $\mathbf{v} = (v_r, v_\theta, v_\phi)$. The governing equations are

$$\frac{\partial \rho}{\partial t} + \nabla \cdot (\rho \mathbf{v}) = 0, \quad (1)$$

$$\frac{\partial(\rho v_r)}{\partial t} + \nabla \cdot (\rho v_r \mathbf{v}) = -\frac{\partial P}{\partial r} - \rho \frac{GM}{r^2} + \rho \frac{v_\theta^2 + v_\phi^2}{r}, \quad (2)$$

$$\frac{\partial(\rho v_\theta)}{\partial t} + \nabla \cdot (\rho v_\theta \mathbf{v}) = -\frac{1}{r} \frac{\partial P}{\partial \theta} - \rho \frac{v_r v_\theta}{r} + \rho \frac{v_\phi^2}{r} \cot \theta, \quad (3)$$

$$\frac{\partial(\rho v_\phi)}{\partial t} + \nabla^l \cdot (\rho v_\phi \mathbf{v}) = 0, \quad (4)$$

$$\frac{\partial E}{\partial t} + \nabla \cdot H \mathbf{v} = -\rho v_r \frac{GM}{r^2} + \rho(\Gamma - \Lambda), \quad (5)$$

$$\frac{\partial n_{\text{H}} y_i}{\partial t} + \nabla \cdot (n_{\text{H}} y_i \mathbf{v}) = n_{\text{H}} R_i. \quad (6)$$

The first five equations are for fluid equations, and the last one means the conservation of chemical species. In the equations, ρ , \mathbf{v} , P , and M_* represent gas density, velocity, pressure, and stellar mass, respectively. The fifth equation is the energy equation. E and H are the total energy and enthalpy including kinetic energy per unit volume. Γ and Λ are the specific heating rate and specific cooling rate, which means the heating and cooling rate per unit mass. The azimuthal component of the Euler equation is described in the angular momentum conservation form. We define y_i as an abundance of chemical species i , n_{H} as the number density of elemental hydrogen, and R_i as a chemical reaction rate. We take into account relevant chemical reactions tabulated in [Nakatani et al. \(2018a,b\)](#). We use PLUTO ([Mignone et al. 2007](#)) to solve hydrodynamics.

We include EUV/X-ray photoionization heating, photoelectric heating ([Bakes & Tielens 1994](#)), dust-gas collisional cooling ([Yorke & Welz 1996](#)), fine-structure cooling of C II and O I ([Hollenbach & McKee 1989; Osterbrock 1989; Santoro & Shull 2006](#)), molecular line cooling of H₂ and CO ([Galli & Palla 1998; Omukai et al. 2010](#)), hydrogen Lyman α line cooling ([Anninos et al. 1997](#)), and radiative recombination cooling ([Spitzer 1978](#)).

Dust temperatures are determined in the same manner as in [Nakatani et al. \(2018a,b\)](#) by performing 2D radiative transfer calculations with a hybrid scheme ([Kuiper et al. 2010; Kuiper & Klessen 2013](#)). Both the direct stellar irradiation and dust re-emission are taken into account. We use the dust opacity of [Draine & Lee \(1984\)](#) that assumes an interstellar dust model.

By running a number of radiation transfer calculations, we have found that the dust temperature distribution is well described by a function of radial distance, R , and column density, N_{H} . The average relative errors are 14% for $M_* = 0.5\text{--}3.0 M_\odot$ and 24% for $M_* = 7.0 M_\odot$, and the error gets relatively large ($\gtrsim 80\%$) at large R where N_{H} is small. However, in such outer low-density regions, the dust temperature is unimportant to determine the gas temperature. Therefore, the error or the inaccuracy of our fitting hardly affects our main results. We use a fitting function for local dust temperatures for each case with different stellar mass ($M_* = 0.5\text{--}7.0 M_\odot$). This significantly saves the computational costs, and thus we are able to follow the long-term evolution of PPDs.

We set the polar angle extent of the computational domains to $0 \leq \theta \leq \pi/2$ rad. We set the radial extent of the computational domains to $0.1r_{\text{g}} \leq r \leq 20r_{\text{g}}$, where r_{g} is the gravitational radius for ionized gas defined by

$$r_{\text{g}} = \frac{GM_*}{(10 \text{ km s}^{-1})^2} \simeq 8.87 \text{ au} \left(\frac{M_*}{1 M_\odot} \right).$$

The radial extent is determined to cover the whole region where photoevaporative flows are expected to be driven ([Liffman 2003](#)), and to avoid spurious reflection of subsonic flows at the outer boundary ([Nakatani et al. 2018a](#)).

In agreement with viscous disk models ([Shakura & Sunyaev 1973; Lynden-Bell & Pringle 1974](#)), the mass accretion rates of low/intermediate-mass stars have been observed to decrease with increasing the age and with decreasing disk mass, M_{disk} (e.g., [Najita et al. 2007; Mendigutía et al. 2012](#)). For the initial condition, we assume evolved systems ($t \gtrsim 10^5\text{--}10^6$ yr), where the main accretion phase has ended and the accretion rate has been dropped (e.g., $\lesssim 1 \times 10^{-8} M_\odot \text{ yr}^{-1}$ for $M_* \leq 1 M_\odot$). In such systems, photoevaporation (or MHD winds) dominates the disk mass loss ([Clarke et al. 2001; Alexander et al. 2006; Owen et al. 2010; Suzuki et al. 2016; Kunitomo et al. 2020](#)). We set the initial disk mass to $M_{\text{disk}}/M_* = 0.03$ (?). The surface density is assumed to scale as $\propto R^{-1}$ ([Andrews et al. 2009](#)). The disk mass within $R_{\text{in}} \leq R \leq R_{\text{out}}$ is

$$M_{\text{disk}} = \int_{R_{\text{in}}}^{R_{\text{out}}} 2\pi R \Sigma(R) \, dR = 2\pi r_{\text{g}} \Sigma_{\text{g}} (R_{\text{out}} - R_{\text{in}}),$$

where Σ_g is the surface density at the gravitational radius, $\Sigma(R) = \Sigma_g(R/r_g)^{-1}$. The inner (R_{in}) and outer (R_{out}) edges of a PPD differ significantly even for systems with similar stellar mass, and likely depend on the formation process, the system's age, and other physical parameters (e.g., Ansdell et al. 2018; Najita & Bergin 2018; Johnston et al. 2020). For the purposes of the present study, we make a practical choice by setting R_{in} at the inner boundary of the computational domain ($0.1r_g$). Since the total disk mass and photoevaporation rates are largely contributed by the outer region, using a smaller R_{in} does not affect these quantities. As for R_{out} , we scale it with r_g to treat “weak-gravity” regions ($R > r_g$) impartially for various stellar mass and set to be equal to the outer boundary of the computational domain ($20r_g$). In this case, Σ_g is computed as

$$\Sigma_g \simeq \frac{M_{\text{disk}}}{40\pi r_g^2} \simeq 27.1 \text{ g cm}^{-2} \left(\frac{M_*}{1 \text{ M}_\odot} \right)^{-1}.$$

The initial gas temperature is given by $T_{\text{ini}} = 100 \text{ K} (R/0.1r_g)^{-1/2}$. We note that the simulation results do not strongly depend on T_{ini} because of rapid gas-dust collisional coupling in optically thick regions.

We run the simulations over a long time of $8.4 \times 10^3 (M_*/\text{M}_\odot) \text{ yr}$, which is 10 times the crossing time of flows having velocities of 1 km s^{-1} ($= 20r_g/1 \text{ km s}^{-1} \approx 8.4 \times 10^2 (M_*/\text{M}_\odot) \text{ yr}$). It is sufficiently long so that the time average of the mass-loss rate converges.

3. RESULTS

3.1. Structure of Photoevaporating Disks

Figure 1 shows the snapshot at $t = 3000 \text{ yr}$ for the run with $M_* = 1.0 \text{ M}_\odot$.

In the right portion, the green region expresses the disk and the blue region is the evaporating gas. Photoevaporative flows come from the surface of the disk where the column density of H_2 satisfies $N(\text{H}_2) = 10^{20} \text{ cm}^{-2}$. We empirically define this boundary as the launching “base” of photoevaporative flows. The temperature at the base depends on the central stellar mass (luminosity), which controls the mass-loss rate. EUV photons heat the gas near the center where $y_{\text{HII}} \geq 0.5$ and the gas temperature $T \geq 3000 \text{ K}$. Adiabatic cooling is the dominant cooling process there.

FUV and X-ray photons heat the gas in the disk interior and drive outflow of a neutral gas. We define Γ_{EUV} , Γ_{FUV} and $\Gamma_{\text{X-ray}}$ as the heating rates by EUV, FUV and X-ray photons, respectively. Figure 2 shows Γ_{FUV} and $\Gamma_{\text{X-ray}}$ at the base. Both the FUV and X-ray heating rates decrease toward the outer part. FUV heating is stronger than X-ray at all distances in the computational domain. This is also the case for simulations with

other stellar masses. The ratio of FUV to X-ray heating $\Gamma_{\text{FUV}}/\Gamma_{\text{X-ray}}$ ranges from 2 to 10 for $M_* = 0.5\text{--}1.7 \text{ M}_\odot$, and the ratio exceeds 1500 for the runs with $M_* = 3.0$ and 7.0 M_\odot . The large heating ratio results from our setting that the increase of X-ray luminosity is smaller than that of FUV luminosity with increasing the stellar mass (see Table 1). Note that the intermediate-mass stars do not have convective zones. The dynamo process of a $M_* = 3.0\text{--}10 \text{ M}_\odot$ star stops at the age of $\sim 1 \text{ Myr}$ (Flaccomio et al. 2003), and the weak magnetic activity on the stellar surface results in X-ray radiation emission. The FUV luminosity can vary according to the accretion rate onto the star. In Section 3.4, We discuss variations of the FUV/X-ray heating rates and the resulting mass-loss rates by running additional simulations with a wide range of stellar luminosities.

Gorti & Hollenbach (2009) argue that FUV heating is the major driver of photoevaporation for PPDs around stars with $M_* = 0.3\text{--}7.0 \text{ M}_\odot$. The temperature at the outflow launching “base” decreases with distance from the central star. We find $\Gamma_{\text{FUV}} \propto (R/r_g)^{-2.0}$ at the base from our simulation results. The X-ray heating rate has similar dependence on the distance from the central star to FUV.

3.2. Photoevaporation Rate

We calculate the mass-loss rate directly from our simulation outputs as

$$\dot{M} = \int_{S, \eta > 0} \rho \mathbf{v} \cdot d\mathbf{S}, \quad (7)$$

where $d\mathbf{S}$ is a spherical surface with radius of $20r_g$. We define η as specific enthalpy

$$\eta = \frac{1}{2} v_p^2 + \frac{1}{2} v_\phi^2 + \frac{\gamma}{\gamma - 1} c_s^2 - \frac{GM_*}{r}. \quad (8)$$

The photoheated gas gains more energy than potential energy and thus evaporates if $\eta > 0$. We include the gas with $\eta > 0$ to calculate the mass-loss rate. The time-averaged mass-loss rates are shown in Figure 3.

The disk mass-loss rate increases with the central star's mass; the relationship is approximated as

$$\dot{M}(r < 20r_g) \simeq 3.69 \times 10^{-9} \left(\frac{M_*}{\text{M}_\odot} \right)^{2.06} \text{ M}_\odot \text{ yr}^{-1} \quad (9)$$

The gas temperature at $r = 1r_g$ on the disk surface is $\simeq 10^3 \text{ K}$ for the run with $M_* = 1 \text{ M}_\odot$ and that around a 7 M_\odot star is $\simeq 8 \times 10^3 \text{ K}$. The average temperature of the gas is higher for heavier central stars.

We set our calculation domain to $0.1r_g \leq r \leq 20r_g$, where r_g is proportional to the central stellar mass. We

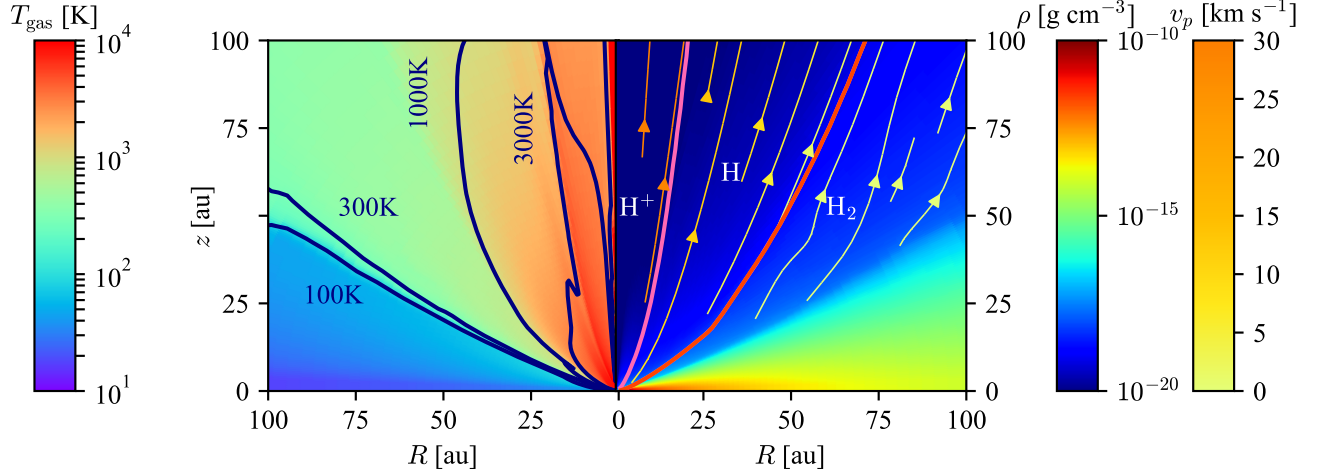


Figure 1. Disk structure at $t = 3000$ yr for the run with $M_* = 1.0 M_\odot$. The color map on the left shows the gas temperature, and the right side shows the density distribution. The navy contour lines on the left show where the gas temperature is 100 K, 300 K, 1000 K, and 3000 K. The right portion also shows the chemical structure of H-bearing species. The pink line on the right represents the ionization front where the abundance of H II is 0.5, and the red line indicates the dissociation front where the abundance of H_2 is 0.25. The streamline represents the poloidal velocity of the gas. v_p expresses the poloidal velocity. For clarity, we omit to plot the streamlines where the velocity is less than 0.1 km s^{-1} , which are mostly seen in the optically thick disk region.

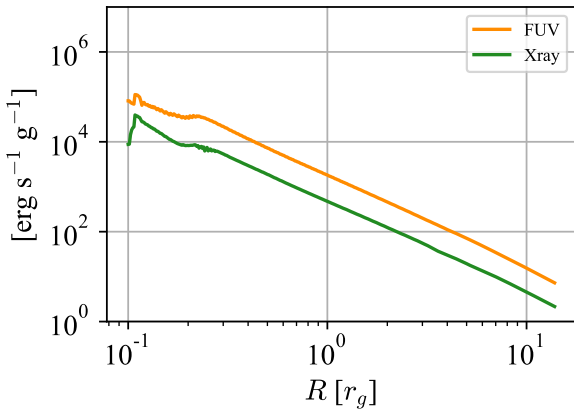


Figure 2. Volume heating rates of FUV photoelectric heating (orange) and the X-ray ionization heating (green) in the model with $M_* = 1.0 M_\odot$. The distance R is in units of r_g .

note that not only the luminosities but also the adopted $R_{\text{out}} (= 20r_g)$ contribute to the stellar mass dependence of the photoevaporation rate in our model. In order to distinguish the effects of R_{out} on the mass-loss rate, we calculate the mass-loss rates by setting the radius of the spherical surface S to 80 au for all of the cases. We find that

$$\dot{M}(r < 80 \text{ au}) \simeq 1.91 \times 10^{-9} \left(\frac{M_*}{M_\odot} \right)^{1.56} M_\odot \text{ yr}^{-1}$$

gives a reasonably accurate fit. The M_* dependence is weak compared to Eq. 9. Nevertheless, the total photoevaporation rates are significantly higher for heavier stars owing to the stronger UV (X-ray) radiation. Previous studies also suggest an apparent increase of photoevaporation rate with the disk radius or measuring radius (Tanaka et al. 2013; Nakatani et al. 2018a; Wölfer et al. 2019).

Gorti & Hollenbach (2009) suggest that the typical mass-loss rate for a disk around a $1.0 M_\odot$ star is $3.0 \times 10^{-8} M_\odot/\text{yr}$, and this is about 3 times larger than our result. The mass-loss rates are consistent with the results of previous studies despite different computational methods. Gorti & Hollenbach (2009) estimate mass-loss rates using a hydrostatic model, while we measure those by performing hydrodynamics simulations. It has also been shown that the X-ray photoevaporation rates differ only by a small factor between hydrostatic and hydrodynamics models (Ercolano et al. 2009; Owen et al. 2010).

We derive a time-averaged surface mass-loss rate, $\dot{\Sigma}(R)$, by differentiating the mass-loss rates with respect to the radius of the spherical surface S . Under steady state, the derivatives correspond to $2\pi R \dot{\Sigma}(R)$ by suitably transforming the spherical radius r to the radial distance R . We show the surface mass-loss rate, $\dot{\Sigma}(R)$, for the simulation with $M_* = 1.0 M_\odot$ in Figure 4. This

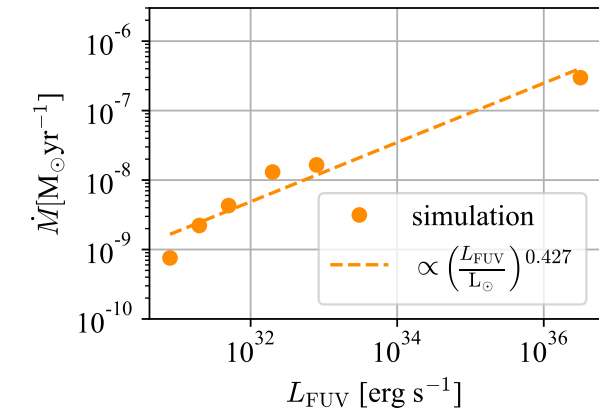
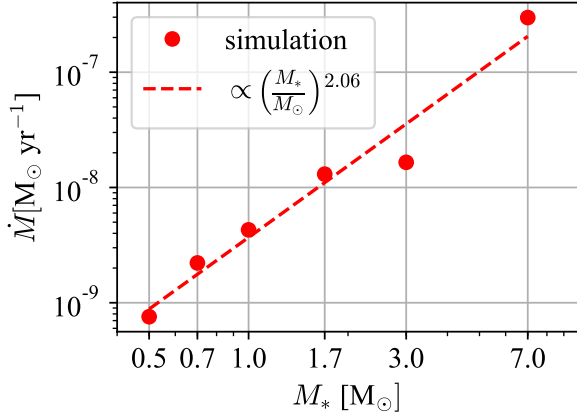


Figure 3. (top) Mass-loss rate with each mass of the central star. The red circles are the simulation data. The red dashed line is a fit. (bottom) Mass-loss rates as a function of FUV luminosity. The orange circles are the simulation data. The lower L_{FUV} corresponds to the lower stellar mass (see Table 1). The orange dotted line is a fit.

figure clarifies which part of the disk evaporates most effectively. The surface mass-loss rate at $M_* = 1.0 \, \text{M}_\odot$ is approximated as

$$\log_{10} \left(\frac{\dot{\Sigma}(R)}{1 \, \text{g s}^{-1} \, \text{cm}^{-2}} \right) = 0.380x^5 - 0.869x^4 + 0.303x^3 + 0.658x^2 - 1.67x - 12.6, \quad (10)$$

where

$$x = \log_{10} \left(\frac{R}{r_g} \right).$$

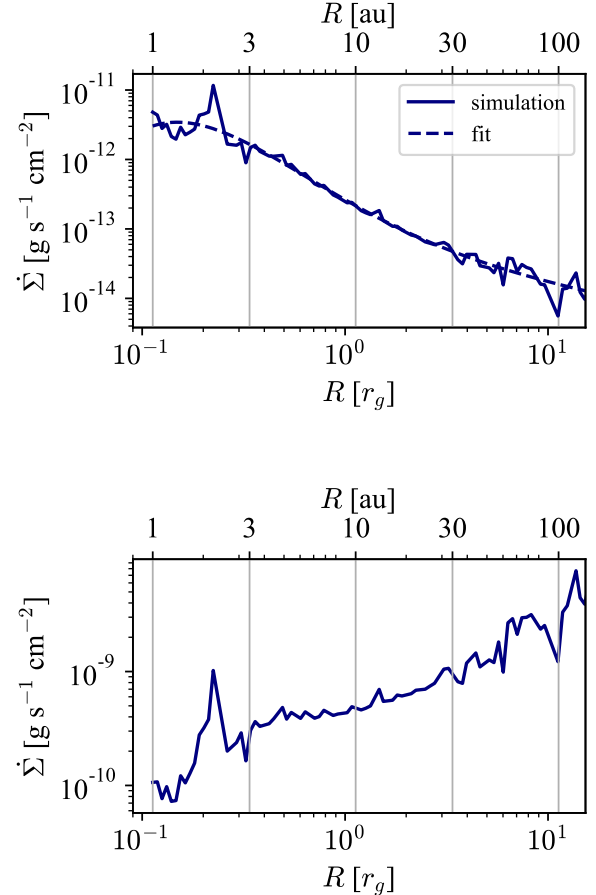


Figure 4. (top) Surface mass-loss rate $\dot{\Sigma}$ for our run with $M_* = 1.0 \, \text{M}_\odot$. The horizontal axes show the radial distance in units of au and r_g at the top and bottom, respectively. The surface mass-loss rate has a peak at $\sim 0.17r_g$ and decreases as the distance from the central star becomes large. The dotted line represents a fit given by equation 10. (bottom) Weighted mass-loss rate $2\pi R^2 \dot{\Sigma}(R)$ with $M_* = 1.0 \, \text{M}_\odot$. The horizontal axes are the same as the top panel.

We approximate $\dot{\Sigma}(R)$ of other stellar masses in the same manner as above

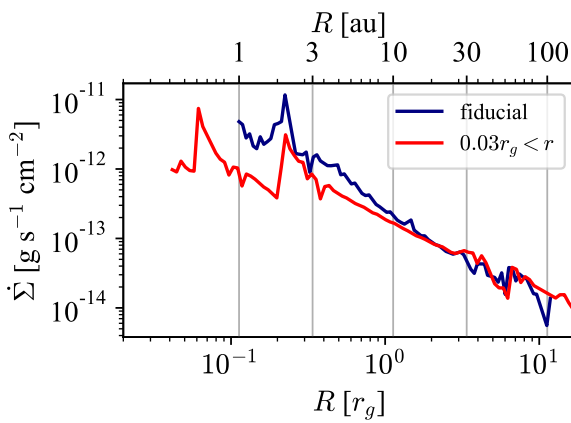
$$\log_{10} \left(\frac{\dot{\Sigma}(R)}{1 \, \text{g s}^{-1} \, \text{cm}^{-2}} \right) = c_5 x^5 + c_4 x^4 + c_3 x^3 + c_2 x^2 + c_1 x + c_0$$

We obtain the fitting coefficients c_0, c_1, c_2, c_3, c_4 , and c_5 as in Table 2.

We define r_{peak} as the radius at which $\dot{\Sigma}$ has the maximum value. In our run with $M_* = 1.0 \, \text{M}_\odot$, the $\dot{\Sigma}$ peaks at $R = 0.17r_g \sim 1.5 \, \text{au}$. The peak position r_{peak} is larger for larger central stellar mass. The peak marks a “boundary” that divides the photoevaporative flows into an FUV-driven region and an EUV-driven region; the

Table 2. The coefficients of $\dot{\Sigma}(R)$

| M_* | c_5 | c_4 | c_3 | c_2 | c_1 | c_0 |
|-------|-------|--------|--------|-------|-------|-------|
| 0.5 | 1.06 | -1.05 | -0.236 | 0.570 | -1.62 | -12.7 |
| 0.7 | 0.693 | -0.95 | -0.038 | 0.678 | -1.67 | -12.6 |
| 1.0 | 0.131 | -0.465 | 0.451 | 0.376 | -1.67 | -12.6 |
| 1.7 | 1.37 | -1.41 | -1.42 | 1.30 | -1.06 | -12.6 |
| 3.0 | 0.033 | -0.786 | 0.786 | 0.557 | -1.58 | -13.1 |
| 7.0 | 0.594 | -1.00 | 0.234 | 0.513 | -1.85 | -12.1 |

**Figure 5.** Comparison of the surface mass-loss rate between the simulations with computational domains of $0.03r_g \leq r \leq 20r_g$ (red) and $0.1r_g \leq r \leq 20r_g$ (blue).

flows are EUV driven inside the peak whereas they are FUV driven outside the peak. The inner, EUV-driven flows have smaller densities than FUV-driven flows, and thus the boundary appears as a peak in the mass-loss profile. We find nonzero mass flux in $R \leq 0.17r_g$. The gravitational binding by the central star is strong in this region, but photoevaporative flows can be launched initially subsonically, which are then accelerated to become supersonic flows as described by a Bernoulli flow model of [Dullemond et al. \(2007\)](#).

In order to see the effects of the choice of inner boundary size on r_{peak} , we run additional simulations setting the computational domain to $0.03r_g \leq r \leq 20r_g$. We show the surface mass-loss rate in Figure 5. We find that photoevaporation occurs also at $r < 0.1r_g$. In the simulation with $0.03r_g \leq r \leq 20r_g$, we find a local maximum in the mass-loss rate profile at the same position ($R \sim 0.17r_g$) as the fiducial one, but also another peak around $r \approx 0.06r_g$, which corresponds to the base density maximum. In the simulation with the small inner boundary, the photoevaporative flows excited from $0.03r_g \leq R \leq 0.1r_g$ shield the stellar radiation that

would have reached the farther outer region. Then, the height of the disk surface where $A_V = 0.5$ increases compared to that in the fiducial run. This difference is significant in terms of density, and thus the surface mass-loss rate is *lower* in $0.2r_g < R < 0.7r_g$ for the simulation with the small inner boundary. We find that, although the disk structure at the innermost region is affected, resolving the inner region does not significantly change the total mass-loss rate.

We calculate $2\pi R^2 \dot{\Sigma}(R)$ based on $\dot{\Sigma}(R)$. This value clarifies the mass loss by photoevaporation at each position. Figure 4 shows how $2\pi R^2 \dot{\Sigma}(R)$ differs by the distance from the central star. The figure shows that the total mass-loss rates are dominated by the outer region. It results in the tendency that the total mass-loss rates increase with the radii at which they are measured.

3.3. Semianalytic Model

We develop a semianalytic model to understand the physical processes that cause the obtained stellar mass dependence of the mass-loss rates. A schematic picture of our model is shown in Figure 6. In this model, the disk is in a steady state, and the photoevaporation flows are excited where the column density of H_2 is $N(\text{H}_2) = 10^{20} \text{ cm}^{-2}$. This is the definition of the base in our model, and is determined empirically from the results of our simulations. The locus of the base is fitted by a function $Z = f(R, M_*) = a(M_*)R^2 + b(M_*)R$ with the fitting coefficients a, b being functions of stellar mass M_* . The flows are launched from the base, having a Mach number of \mathcal{M} and launching angle β with respect to the base. The azimuthal velocity is simply assumed to be $v_\phi = \sqrt{GM_*/r}$ at the base. Following Eq. 7, the launched photoevaporated flows are regarded as gravitationally unbound if $\eta > 0$.

The coefficients for $f(R, M_*)$ are found to be

$$a(M_*) = \left[3.81 \times 10^{-5} \left(\frac{M_*}{\text{M}_\odot} \right)^2 - 5.44 \times 10^{-3} \left(\frac{M_*}{\text{M}_\odot} \right) + 4.58 \times 10^{-2} \right] \times r_g^{-1}$$

$$b(M_*) = 9.78 \times 10^{-1} \left(\frac{M_*}{\text{M}_\odot} \right) + 9.74 \times 10^{-3}.$$

We derive the base temperature of our model by directly fitting our simulation results as

$$T_{\text{fit}} = T_0(M_*) \left(\frac{r}{r_g} \right)^{\alpha(M_*)},$$

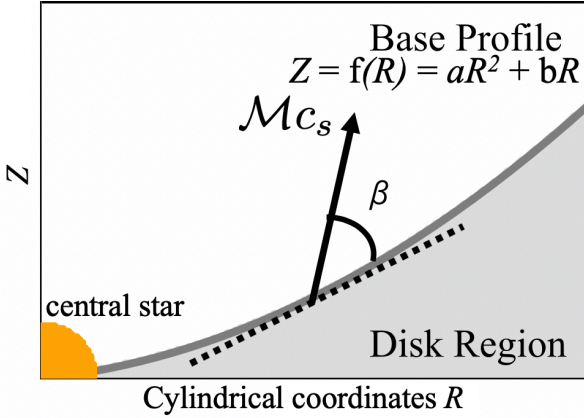


Figure 6. Configuration in our analytic model. We approximate the shape of the disk to be a quadratic function. The photoevaporative flows are launched at the speed $\mathcal{M}c_s$. We set the angle between the direction of the gas velocity and the base as β .

where we find

$$T_0 = 1.30 \times 10^3 + 2.79 \times 10^2 \left(\frac{M_*}{M_\odot} \right) \text{ K}$$

$$\alpha(M_*) = 8.92 \times 10^{-1} \left(\frac{M_*}{M_\odot} \right)^{-0.108}.$$

Similarly, we fit the base density of our simulations as

$$\rho_{\text{fit}} = \rho_0(M_*) \left(\frac{r}{r_g} \right)^{c(M_*)},$$

where

$$\rho_0(M_*) = 3.03 \times 10^{-18} \left(\frac{M_*}{M_\odot} \right)^{-0.309} \text{ g cm}^{-3}$$

$$c(M_*) = 3.60 \times 10^{-3} \left(\frac{M_*}{M_\odot} \right)^3 - 2.55 \times 10^{-2} \left(\frac{M_*}{M_\odot} \right)^2$$

$$- 4.42 \times 10^{-2} \left(\frac{M_*}{M_\odot} \right) - 0.640.$$

With the assumptions of our model, Eq. 8 reduces to

$$\eta = \frac{1}{2} \mathcal{M}^2 c_s^2 + \frac{\gamma}{\gamma - 1} c_s^2 - \frac{GM_*}{2r}$$

at the base, and the photoevaporation condition, $\eta > 0$, is rewritten as

$$r > r_{\min} = r_g \left[\frac{\gamma - 1}{(\gamma - 1)\mathcal{M}^2 + 2\gamma} \frac{\mu m_H G M_*}{k T_0 r_g} \right]^{\frac{1}{1+\alpha}}.$$

This can be interpreted as the heated gas being unbound at $r > r_{\min}$. Note that r_{\min} is defined in spherical polar coordinates. The corresponding cylindrical

radius, R_{\min} , is given by the positive root of the equation, $r_{\min}^2 = R_{\min}^2 + [f(R_{\min}, M_*)]^2$. We find that \mathcal{M} and β are not strongly dependent on the distance from the central star. The averaged \mathcal{M} and β are

$$\bar{\mathcal{M}} = 0.35 \times \left(\frac{M_*}{M_\odot} \right)^{0.40},$$

$$\sin \bar{\beta} = 0.5,$$

respectively. We adopt these values for our semianalytic model.

The cumulative photoevaporation rate within R is computed by integrating the effective mass flux with respect to R ,

$$\dot{M}_{\text{model}} = 2 \times \int_{R_{\min}}^R ds 2\pi R \rho v_p \sin \beta,$$

where ds is the line element of the base ($ds = \sqrt{1 + f'^2} dR$). The gradient of f is given by an average as $\bar{f}' = (f(R) - f(R_{\min}))/ (R - R_{\min})$. Substituting the fit for relevant quantities, we obtain

$$\dot{M}_{\text{model}}(< R) = \frac{8\pi \bar{\mathcal{M}} \sin \bar{\beta} \rho_0 \sqrt{k T_0 / \mu m_H} \sqrt{1 + \bar{f}'^2}}{(\bar{f}'^2 + b\bar{f}' + 2)(2 + c + \alpha/2)}$$

$$\times r_g^2 \left(\frac{r_{\max}/r_g}{\sqrt{1 + \bar{f}'^2}} \right)^{2+c+\alpha/2} \left[1 - \left(\frac{r_{\min}}{r_{\max}} \right)^{2+c+\alpha/2} \right]$$

$$\simeq 2.97 \times 10^{-10} M_\odot \text{ yr}^{-1} \left(\frac{M_*}{M_\odot} \right)^{2.40} \left(\frac{r_{\max}/r_g}{\sqrt{1 + \bar{f}'^2}} \right)^{2+c+\alpha/2}$$

$$\times \rho_{18} T_3^{1/2} \frac{\sqrt{1 + \bar{f}'^2} \left[1 - (r_{\min}/r_{\max})^{2+c+\alpha/2} \right]}{(\bar{f}'^2 + b\bar{f}' + 2)(2 + c + \alpha/2)},$$

where $r_{\max} \equiv \sqrt{R^2 + [f(R^2, M_*)]^2}$, $\rho_{18} \equiv \rho_0/10^{-18} \text{ g cm}^{-3}$, and $T_3 \equiv T_0/10^3 \text{ K}$. In Figure 7, we compare the analytic mass-loss rates within $r < 20r_g$ with those of the simulations.

The semianalytic model can accurately reproduce the simulation results. Note that the contribution of the mass flux within $< r_{\min}$ is 1–4% of the total mass-loss rates in our simulations. Therefore, the mass-loss rates of the model and simulations are fairly in good agreement despite the fact that the model ignores the contribution of the hot gas from $< r_{\min}$.

3.4. Luminosity Dependence

The FUV, EUV, and X-ray luminosities of young stars are not tightly constrained by observations, mainly because of uncertain interstellar extinction. The luminosities are likely different among the same spectral-type

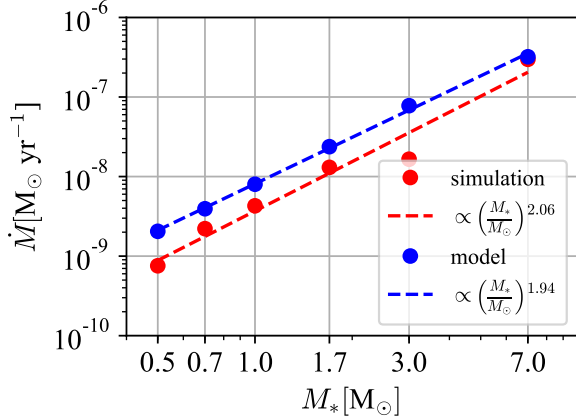


Figure 7. Mass-loss rates as a function of the host star mass. The red dots are the simulation results, and the blue dots shows the model photoevaporation rate. The dashed lines with the corresponding colors show power-law fits.

stars, and can also depend on other stellar properties such as age, magnetic activities, and accretion rate (e.g., Gullbring et al. 1998; Preibisch et al. 2005; Ingleby et al. 2011; Güdel et al. 2007; Yang et al. 2012; Schindhelm et al. 2012; France et al. 2012; Vidotto et al. 2014; France et al. 2018, ; see also Alexander et al. (2014) for review). In order to examine the effects of the assumed luminosities on our results, we perform additional simulations for $M_* = 1 \text{ M}_\odot$ but with varying each of FUV, EUV, and X-ray luminosities by 0.01, 0.1, 10, and 100 times of the fiducial value. The resulting mass-loss rates are $7.5\text{--}9.0 \times 10^{-9} \text{ M}_\odot \text{ yr}^{-1}$ when varying the EUV luminosity. Clearly, the mass-loss rate is insensitive to the EUV luminosity. In contrast, the mass-loss rate increases with increasing FUV and X-ray luminosities as shown in Figure 8. We find an approximate dependence of

$$\dot{M} \simeq 3.86 \times 10^{-9} \left(\frac{L_{\text{FUV}}}{L_{\text{FUV,f}}} \right)^{0.518} \text{ M}_\odot \text{ yr}^{-1} \quad (11)$$

$$\dot{M} \simeq 5.90 \times 10^{-9} \left(\frac{L_{\text{X-ray}}}{L_{\text{X-ray,f}}} \right)^{0.257} \text{ M}_\odot \text{ yr}^{-1}, \quad (12)$$

where $L_{\text{FUV,f}}$ and $L_{\text{X-ray,f}}$ are the fiducial values (Table 1). X-ray is responsible for the mass-loss rate for $L_{\text{FUV}}/L_{\text{FUV,f}} = 0.01$ and $L_{\text{X-ray}}/L_{\text{X-ray,f}} \gtrsim 10$. In the Appendix A, we provide fits to the surface mass-loss rates of the simulations with various luminosities. The FUV and X-ray heating rates are comparable when $L_{\text{FUV}}/L_{\text{FUV,f}} \approx 0.05$ ($L_{\text{FUV}}/L_{\text{X}} \sim 1$). The higher $L_{\text{FUV}}/L_{\text{X}}$ ratio in our fiducial runs promotes FUV heating that dominates over X-ray heating (see Figure 2).

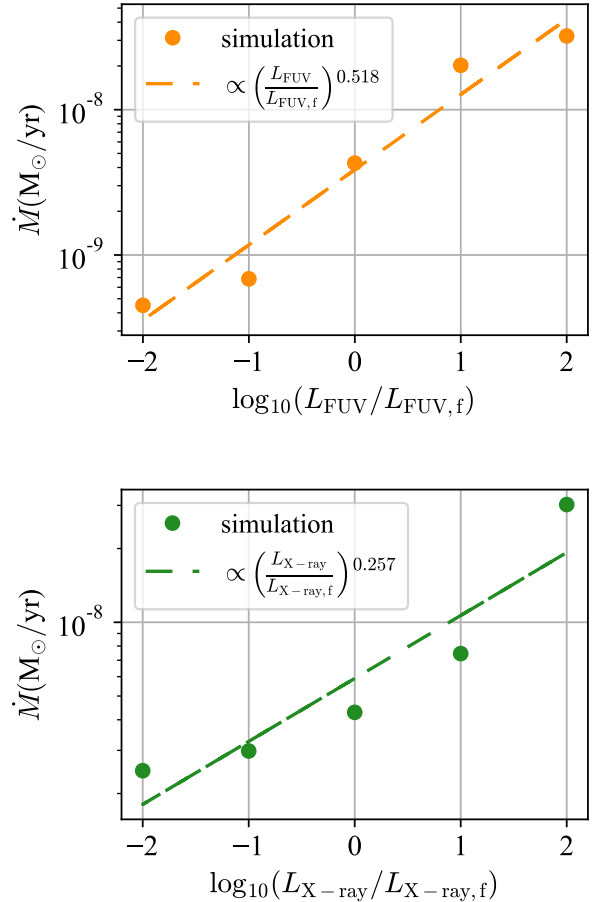


Figure 8. (top) Mass-loss rate with each FUV luminosity and $M_* = 1.0 \text{ M}_\odot$. The orange points are the simulation data. The orange dashed line is a fit. (bottom) Mass-loss rate with each X-ray luminosity and $M_* = 1.0 \text{ M}_\odot$. The green points are the simulation data. The green dashed line is a fit. L_f is a fiducial value defined in Table 1

It is worth comparing our results with those of previous studies. ? run hydrodynamics simulations with varying X-ray luminosities. They find that the mass-loss rate scales with $L_{\text{X-ray}}$ more steeply than our result (Figure 8). In our model, photoevaporation is predominantly driven by FUV radiation when the X-ray luminosity is low, and thus the mass-loss rate does not scale strongly with the X-ray luminosity if $L_{\text{X-ray}}/L_{\text{X-ray,f}} \lesssim 10$. This leads to apparently different X-ray luminosity dependence from that of ?. On the other hand, with strong X-ray radiation, the disk heating is dominated by X-ray, and the mass-loss rate increases as $\dot{M} \propto (L_{\text{X-ray}}/L_{\text{X-ray,f}})^{0.6}$, which is close to the result of ?.

Since the FUV luminosity decreases as the accretion rate decreases, X-ray heating would become important

at later phases of the disk evolution. Note, however, that there are several other effects that can affect the relative dominance of the FUV/EUV/X-ray heating. For instance, grain growth and the stellar evolution itself can affect the heating efficiencies in a complicated manner. Including those effects would be necessary to fully understand the chronological variability of the disk structure and the mass-loss rate.

4. DISCUSSION

4.1. Dispersal Time of Inner Disks

Previous 1D disk evolution models suggest that the surface density evolution is governed by viscous evolution at an early stage. When the accretion rate decreases comparable to the photoevaporation rate, a gap opens at around the gravitational radius, which separates the initially smooth disk into the inner and outer disks (e.g., Clarke et al. 2001; Alexander et al. 2006; Owen et al. 2010). The inner disk quickly accretes onto the central star on the viscous timescale, while the outer disk is dispersed by photoevaporation on a relatively short time compared to the disk lifetime. In this section, we estimate the inner-disk lifetimes using the photoevaporation rates we have derived so far. We compare them with those estimated by infrared observations.

We define the inner-disk lifetime as the time at which the accretion rate decreases to the photoevaporation rate. Following Clarke et al. (2001), we introduce the viscous scaling time

$$t_s = \frac{M_{\text{disk},0}}{2\dot{M}_{\text{acc},0}},$$

where $M_{\text{disk},0}$ and $\dot{M}_{\text{acc},0}$ are the initial disk mass and the initial rate of accretion onto the star, respectively. The accretion rate decays as $\propto t^{-3/2}$ for $t \gg t_s$. Thus, the timescale t_w over which \dot{M}_{acc} decreases to \dot{M} can be derived by solving

$$\dot{M} \approx \dot{M}_{\text{acc},0} \left(\frac{t}{t_s} \right)^{-3/2} \quad (13)$$

with respect to t (Clarke et al. 2001). In our fiducial model, \dot{M} is determined by FUV-driven photoevaporative flows. The adopted accretion rate has is $\dot{M}_{\text{acc}} = 3 \times 10^{-8} (M_*/M_\odot)^2 M_\odot \text{ yr}^{-1}$ (Muzerolle et al. 2003; Gorti & Hollenbach 2009) which is assumed to be that of a 1 Myr-old system (Gorti & Hollenbach 2009). The accretion rate is supposed to be significantly higher at an earlier stage of the disk evolution. The FUV luminosity and thereby \dot{M} are also expected to be higher at that time and to be time dependent. To incorporate this effect into our discussion here, we assume $L_{\text{FUV}} \propto \dot{M}_{\text{acc}}$

(e.g., Calvet & Gullbring 1998; Gullbring et al. 1998) and $\dot{M} \propto L_{\text{FUV}}^\lambda$ ($0 < \lambda < 1$; see Eq. 11). These assumptions reduce Eq. 13 to

$$t_w = t_s \left[\frac{\dot{M}_{\text{acc},0}}{\dot{M}(1 \text{ Myr})} \left(\frac{\dot{M}_{\text{acc}}(1 \text{ Myr})}{\dot{M}_{\text{acc},0}} \right)^\lambda \right]^{2/3(1-\lambda)},$$

where $\dot{M}_{\text{acc}}(1 \text{ Myr}) = 3 \times 10^{-8} (M_*/M_\odot)^2 M_\odot \text{ yr}^{-1}$, and $\dot{M}(1 \text{ Myr})$ is the photoevaporation rate obtained in this study. Since t_w is determined for given $M_{\text{disk},0}$ and $\dot{M}_{\text{acc},0}$, we treat the latter two quantities as parameters in the following discussion. We adopt the power-law index of Eq. 11 for λ .

The resulting t_w are shown in Figure 9. We have considered three parameter sets:

$$(M_{\text{disk},0}, \dot{M}_{\text{acc},0}) = \begin{cases} (0.1 M_*, 3.0 \times 10^{-7} M_\odot \text{ yr}^{-1}) \\ (0.06 M_*, 3.0 \times 10^{-7} M_\odot \text{ yr}^{-1}) \\ (0.1 M_*, 1.0 \times 10^{-6} M_\odot \text{ yr}^{-1}) \end{cases}.$$

These models are labeled as “Md0.1Macc3e-7”, “Md0.06Macc3e-7”, and “Md0.1Macc3e-6” in Figure 9, and are shown as blue, red, and orange circles, respectively. The derived t_w , our proxy for the inner-disk lifetime, is shorter for the models that yield a higher mass-loss rate (Figure 3).

In the discussion above, we have followed Clarke et al. (2001) and have assumed a viscosity profile of $\nu \propto R$. We can also consider different radial profiles as $\nu \propto R^\kappa$, to examine the uncertainty in the derived lifetimes. To this end, we adopt a generalized model of ? and rewrite Eq. 13 as

$$\dot{M} \approx \dot{M}_{\text{acc},0} \left(\frac{t}{t_s} \right)^{-(5/2-\kappa)/(2-\kappa)}.$$

Then, the inner-disk lifetime is expressed as

$$t_w = t_s \left[\frac{\dot{M}_{\text{acc},0}}{\dot{M}(1 \text{ Myr})} \left(\frac{\dot{M}_{\text{acc}}(1 \text{ Myr})}{\dot{M}_{\text{acc},0}} \right)^\lambda \right]^\chi$$

$$\chi = \frac{(2-\kappa)}{(5/2-\kappa)(1-\lambda)}.$$

If we adopt $\kappa = 3/2$ as in one of the variable α -viscosity model of ?, the resulting lifetime becomes twice as short as the fiducial value, but the stellar mass dependence remains essentially unaffected.

In Figure 9, we also plot the inner-disk lifetimes estimated from the observational disk fractions compiled in Bayo et al. (2012) and Ribas et al. (2015). Bayo et al. (2012) provide a mass function of the disk fractions obtained by infrared excess observations toward the young

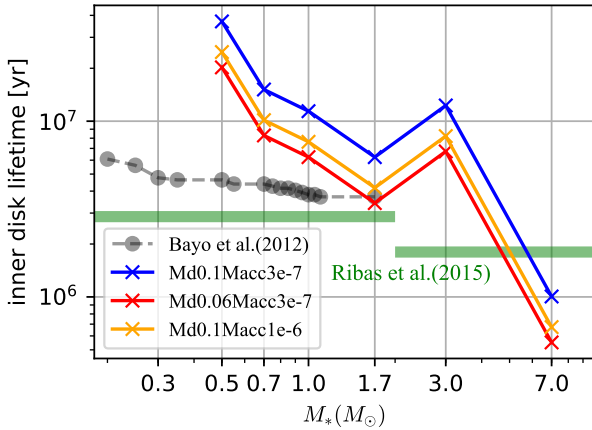


Figure 9. Inner-disk lifetimes. The blue, red, and orange solid lines are those derived with assuming the initial disk mass and the accretion rate onto the star as $(M_{\text{disk},0}, \dot{M}_{\text{acc},0}) = (0.1 M_*, 3.0 \times 10^{-7} M_\odot \text{ yr}^{-1})$, $(0.06 M_*, 3.0 \times 10^{-7} M_\odot \text{ yr}^{-1})$, $(0.1 M_*, 1.0 \times 10^{-6} M_\odot \text{ yr}^{-1})$, respectively. The black points and green horizontal bars represent inner-disk lifetimes estimated from observational disk fractions in Bayo et al. (2012) and Ribas et al. (2015), respectively. See the main text for more detail.

cluster Collinder 69 in the Lambda Orionis star-forming region. The disk fraction at a mass bin M_i is defined as the ratio of the disk-bearing members to the total members in $M_* < M_i$. Although this definition does not give the specific disk fraction at $M_* = M_i$, we use the disk fractions of Bayo et al. (2012) as an approximate substitute of the specific disk fraction; otherwise, the number of samples is too small to be statistically meaningful in each mass bin. We convert the disk fraction to lifetime in an approximate manner as

$$t_{\text{life}} = -\frac{t_{\text{age}}}{\ln f_{\text{disk}}},$$

where f_{disk} is the disk fraction and t_{age} is the age of the star-forming region ($t_{\text{age}} = 5 \text{ Myr}$; Bayo et al. 2011). The resulting lifetimes are shown by the gray circles in Figure 9. Ribas et al. (2015) derive the disk fractions using a large sample across various star-forming regions whose ages are in the range of $\sim 1\text{--}11 \text{ Myr}$. The samples are categorized into low-mass ($M_* < 2 M_\odot$) and high-mass ($M_* > 2 M_\odot$) sources. Each group is further classified into young (1–3 Myr) and old (3–11 Myr) sources, and the disk fractions are derived for each of the four categories. We approximately estimate the lifetimes of the low-mass and high-mass sources by fitting the disk fractions as a function of age

$$f(t) = \exp \left[-\frac{t}{t_{\text{life}}} \right].$$

Each of the age bins has a wide spread. Therefore, we take the medians, 2 Myr and 7 Myr for the young and old groups, respectively, as representative ages. The resulting lifetimes are represented by the green horizontal bars in Figure 9.

The stellar mass dependence of the estimated inner-disk lifetimes is overall consistent with the observations. The inner-disk lifetimes are estimated to be much longer than the observations for $M_* \leq 1.7 M_\odot$. This may indicate that other processes, such as MHD winds and planet formation, contribute to dispersing the disks in this stellar mass range. Interestingly, recent 1D simulations that implement all of accretion, photoevaporation, and MHD winds suggest that MHD winds drive a major mass loss at the early epoch of the evolution at least for solar-type stars (Kunitomo et al. 2020, Fukuhara in prep.). We also find that the inner-disk lifetimes are long for $M_* \sim 3 M_\odot$. This suggests that the stellar (evolutionary) property can cause a non-monotonic dependence of the lifetimes on the stellar mass. The estimated lifetimes are significantly short at $M_* > 3 M_\odot$ because the strong photoevaporation disperses the disk quickly around a high-mass star.

4.2. Uncertainties of Model Parameters

The abundance of PAHs and small grains is critical for FUV photoelectric heating and hence FUV-driven photoevaporation (Gorti & Hollenbach 2008, 2009; Gorti et al. 2015; Nakatani et al. 2018a). The dust abundance can vary significantly through grain growth and destruction by the stellar UV and X-ray radiation (Siebenmorgen & Krügel 2010; Vicente et al. 2013). Observationally, the PAH abundance is poorly constrained, but it has been suggested to be smaller than the interstellar value (Geers et al. 2007; Oliveira et al. 2010). Gorti et al. (2015) show that dust growth indeed results in weakening FUV photoevaporation, but FUV radiation is still effective enough to drive mass loss with the reduced PAH and small grain abundances by a factor of $\sim 10\text{--}100$. This is also expected in our model, and thus the derived dispersal time would not be strongly affected by taking into account reduced abundances of PAHs and small grains. Note that, for further lower dust abundances, X-ray heating is the primary process that drives mass loss.

4.3. Other Effects

Figure 9 shows a stellar mass dependence of dispersal time caused by *internal* photoevaporation. Photoevaporation by external radiation sources has been suggested to shape the mass functions of disk masses in star-forming regions by recent submillimeter surveys

(Ansdel et al. 2018). Distance from the external UV source(s) and the disk size (the geometrical cross section to the radiation field) are key parameters to determine the mass-loss rate in such cases (Johnstone et al. 1998; Störzer & Hollenbach 1999; Hollenbach et al. 2000). It would be important to incorporate the effects of external photoevaporation to address the disk lifetime quantitatively, particularly for massive star-forming regions. The derived mass-loss rates in this study apply to the systems where internal photoevaporation dominates mass loss.

We have derived the disk-dispersal time by a scaling argument on the basis of physical processes. In practice, accretion and MHD winds can also contribute considerably to the mass evolution. These effects are responsible for angular momentum redistribution and dominate mass loss especially at an early evolutionary stage of protoplanetary disks (Suzuki et al. 2016; Kunitomo et al. 2020). As discussed in Section 4.1, disk accretion is also an important process to determine the overall impact of FUV-driven photoevaporation. When the system evolves and the accretion rate drops, the photoevaporation rate can also decrease owing to the reduced FUV contribution from the accretion. Furthermore, the stellar FUV/EUV/X-ray luminosities can vary depending on detailed processes and phases in the stellar evolution such as development of the convective zone and changes in the photospheric temperature. Incorporating these variable processes over the evolution of the system would also significantly affect the disk-dispersal process and the stellar mass dependence.

For more detailed comparisons between our model and observations, it may be necessary to follow a long-term evolution including a variety of physical processes.

5. SUMMARY

Recent observations suggest that the lifetime of a PPD depends on the central stellar mass. Theoretically, disk photoevaporation can cause such dependence because the luminosity of the central star increases with the stellar mass. On the other hand, stronger gravity of heavier

stars may prevent efficient disk mass loss, and the details of the disk-dispersal mechanism remain unknown. We have performed a suite of radiation hydrodynamics simulations to investigate the disk lifetime. Our simulations show that the mass-loss rate increases with M_* as $\dot{M} = 3.69 \times 10^{-9} (M_*/M_\odot)^{2.06} M_\odot \text{ yr}^{-1}$.

Based on the simulation results, we have developed a semianalytic model that reproduces the disk mass-loss rates accurately. We derive the surface mass-loss rates for a variety of cases and provide simple polynomial functional fits. The results are aimed at being used by semianalytic studies of the evolution of PPDs. We have found that there is a nonzero contribution to the mass-loss rate even within $r < r_g$. We have estimated the inner-disk lifetime from the resulting photoevaporation rate. The estimated inner-disk lifetime is consistent with the proposed observational trend of the stellar mass dependence, where the lifetimes are shorter for higher-mass stars.

Our radiation hydrodynamics simulations show that disk photoevaporation can explain the observed correlation between disk lifetime and the host star mass. We have not included the effects of accretion, MHD winds, and external radiation sources in the present study. In future work, we will study the long-term evolution of PPDs including these effects and make a comparison with observations.

ACKNOWLEDGMENTS

We thank Takeru Suzuki and Masahiro Ogihara for fruitful discussions. R.N. acknowledges support from the Special Postdoctoral Researcher program at RIKEN and from Grant-in-Aid for Research Activity Start-up (19K23469). Numerical computations were carried out on Cray XC50 at Center for Computational Astrophysics, National Astronomical Observatory of Japan

APPENDIX

Table 3. The coefficients of $\dot{\Sigma}(R)$

| Luminosity | c_8 | c_7 | c_6 | c_5 | c_4 | c_3 | c_2 | c_1 | c_0 |
|----------------------------------|-------|--------|-------|--------|-------|-------|--------|-------|-------|
| $L_{\text{FUV,f}} \times 0.01$ | -6.90 | 6.04 | 9.87 | -7.81 | -3.22 | 2.46 | -0.124 | -1.10 | -13.3 |
| $L_{\text{FUV,f}} \times 0.1$ | -12.7 | 10.4 | 18.0 | -14.0 | -6.32 | 5.80 | 0.347 | -1.90 | -13.2 |
| $L_{\text{FUV,f}} \times 10$ | -2.91 | 4.62 | 3.02 | -6.82 | 0.325 | 2.49 | -0.732 | -1.16 | -11.7 |
| $L_{\text{FUV,f}} \times 100$ | -14.1 | 21.5 | 11.3 | -24.6 | -1.19 | 8.33 | -0.273 | -2.15 | -11.2 |
| $L_{\text{X-ray,f}} \times 0.01$ | -7.36 | 6.47 | 8.34 | -6.88 | -1.68 | 1.87 | -0.32 | -1.18 | -12.6 |
| $L_{\text{X-ray,f}} \times 0.1$ | -3.50 | -0.029 | 7.08 | -0.422 | -3.67 | 0.695 | 0.166 | -1.34 | -12.4 |
| $L_{\text{X-ray,f}} \times 10$ | 6.67 | -3.94 | -15.0 | 7.69 | 8.43 | -2.95 | -1.14 | -1.31 | -12.0 |
| $L_{\text{X-ray,f}} \times 100$ | -5.43 | -2.02 | 10.0 | 1.34 | -5.95 | 0.637 | 1.31 | -1.38 | -11.5 |

A. MASS LOSS PROFILES FOR VARIOUS INPUT LUMINOSITIES

We calculate the surface mass-loss rates for various FUV and X-ray luminosities considered in Section 3.4. We fit $\dot{\Sigma}(R)$ by

$$\log_{10} \left(\frac{\dot{\Sigma}(R)}{1 \text{ g s}^{-1} \text{ cm}^{-2}} \right) = c_8 x^8 + c_7 x^7 + c_6 x^6 + c_5 x^5 + c_4 x^4 + c_3 x^3 + c_2 x^2 + c_1 x + c_0$$

where

$$x = \log_{10} \left(\frac{R}{r_g} \right).$$

Here we resort to higher-order polynomial fitting than that of (10) because we have found that Eq. 10 does not provide accurate fits to $\dot{\Sigma}(R)$. We list the obtained fitting coefficients ($c_0, c_1, c_2, c_3, c_4, c_5, c_6, c_7$, and c_8) in Table 3.

REFERENCES

Alexander, R., Pascucci, I., Andrews, S., Armitage, P., & Cieza, L. 2014, in Protostars and Planets VI, ed. H. Beuther, R. S. Klessen, C. P. Dullemond, & T. Henning, 475, doi: [10.2458/azu_uapress_9780816531240-ch021](https://doi.org/10.2458/azu_uapress_9780816531240-ch021)

Alexander, R. D., Clarke, C. J., & Pringle, J. E. 2006, MNRAS, 369, 229, doi: [10.1111/j.1365-2966.2006.10294.x](https://doi.org/10.1111/j.1365-2966.2006.10294.x)

Allers, K. N., Jaffe, D. T., Luhman, K. L., et al. 2007, ApJ, 657, 511, doi: [10.1086/510845](https://doi.org/10.1086/510845)

Andrews, S. M., Wilner, D. J., Hughes, A. M., Qi, C., & Dullemond, C. P. 2009, ApJ, 700, 1502, doi: [10.1088/0004-637X/700/2/1502](https://doi.org/10.1088/0004-637X/700/2/1502)

Anninos, P., Zhang, Y., Abel, T., & Norman, M. L. 1997, NewA, 2, 209, doi: [10.1016/S1384-1076\(97\)00009-2](https://doi.org/10.1016/S1384-1076(97)00009-2)

Ansdel, M., Williams, J. P., Manara, C. F., et al. 2017, AJ, 153, 240, doi: [10.3847/1538-3881/aa69c0](https://doi.org/10.3847/1538-3881/aa69c0)

Ansdel, M., Williams, J. P., van der Marel, N., et al. 2016, ApJ, 828, 46, doi: [10.3847/0004-637X/828/1/46](https://doi.org/10.3847/0004-637X/828/1/46)

Ansdel, M., Williams, J. P., Trapman, L., et al. 2018, ApJ, 859, 21, doi: [10.3847/1538-4357/aab890](https://doi.org/10.3847/1538-4357/aab890)

Bakes, E. L. O., & Tielens, A. G. G. M. 1994, ApJ, 427, 822, doi: [10.1086/174188](https://doi.org/10.1086/174188)

Bayo, A., Barrado, D., Huélamo, N., et al. 2012, A&A, 547, A80, doi: [10.1051/0004-6361/201219374](https://doi.org/10.1051/0004-6361/201219374)

Bayo, A., Barrado, D., Stauffer, J., et al. 2011, A&A, 536, A63, doi: [10.1051/0004-6361/201116617](https://doi.org/10.1051/0004-6361/201116617)

Bergin, E., Calvet, N., D'Alessio, P., & Herczeg, G. J. 2003, ApJL, 591, L159, doi: [10.1086/377148](https://doi.org/10.1086/377148)

Calvet, N., & Gullbring, E. 1998, ApJ, 509, 802, doi: [10.1086/306527](https://doi.org/10.1086/306527)

Carpenter, J. M., Mamajek, E. E., Hillenbrand, L. A., & Meyer, M. R. 2006, ApJL, 651, L49, doi: [10.1086/509121](https://doi.org/10.1086/509121)

Clarke, C. J., Gendrin, A., & Sotomayor, M. 2001, MNRAS, 328, 485, doi: [10.1046/j.1365-8711.2001.04891.x](https://doi.org/10.1046/j.1365-8711.2001.04891.x)

Dahm, S. E., & Hillenbrand, L. A. 2007, AJ, 133, 2072, doi: [10.1086/512156](https://doi.org/10.1086/512156)

Draine, B. T., & Lee, H. M. 1984, ApJ, 285, 89, doi: [10.1086/162480](https://doi.org/10.1086/162480)

Dullemond, C. P., Hollenbach, D., Kamp, I., & D'Alessio, P. 2007, in *Protostars and Planets V*, ed. B. Reipurth, D. Jewitt, & K. Keil, 555.
<https://arxiv.org/abs/astro-ph/0602619>

Ercolano, B., Clarke, C. J., & Drake, J. J. 2009, *ApJ*, 699, 1639, doi: [10.1088/0004-637X/699/2/1639](https://doi.org/10.1088/0004-637X/699/2/1639)

Fang, M., van Boekel, R., King, R. R., et al. 2012, *A&A*, 539, A119, doi: [10.1051/0004-6361/201015914](https://doi.org/10.1051/0004-6361/201015914)

Flaccomio, E., Damiani, F., Micela, G., et al. 2003, *ApJ*, 582, 398, doi: [10.1086/344536](https://doi.org/10.1086/344536)

France, K., Arulanantham, N., Fossati, L., et al. 2018, *ApJS*, 239, 16, doi: [10.3847/1538-4365/aae1a3](https://doi.org/10.3847/1538-4365/aae1a3)

France, K., Schindhelm, E., Herczeg, G. J., et al. 2012, *ApJ*, 756, 171, doi: [10.1088/0004-637X/756/2/171](https://doi.org/10.1088/0004-637X/756/2/171)

Galli, D., & Palla, F. 1998, *A&A*, 335, 403.
<https://arxiv.org/abs/astro-ph/9803315>

Geers, V. C., van Dishoeck, E. F., Visser, R., et al. 2007, *A&A*, 476, 279, doi: [10.1051/0004-6361:20078466](https://doi.org/10.1051/0004-6361:20078466)

Gorti, U., & Hollenbach, D. 2008, *ApJ*, 683, 287, doi: [10.1086/589616](https://doi.org/10.1086/589616)

—. 2009, *ApJ*, 690, 1539, doi: [10.1088/0004-637X/690/2/1539](https://doi.org/10.1088/0004-637X/690/2/1539)

Gorti, U., Hollenbach, D., & Dullemond, C. P. 2015, *ApJ*, 804, 29, doi: [10.1088/0004-637X/804/1/29](https://doi.org/10.1088/0004-637X/804/1/29)

Gressel, O., Ramsey, J. P., Brinch, C., et al. 2020, *ApJ*, 896, 126, doi: [10.3847/1538-4357/ab91b7](https://doi.org/10.3847/1538-4357/ab91b7)

Güdel, M., Briggs, K. R., Arzner, K., et al. 2007, *A&A*, 468, 353, doi: [10.1051/0004-6361:20065724](https://doi.org/10.1051/0004-6361:20065724)

Gullbring, E., Hartmann, L., Briceño, C., & Calvet, N. 1998, *ApJ*, 492, 323, doi: [10.1086/305032](https://doi.org/10.1086/305032)

Haisch, Karl E., J., Lada, E. A., & Lada, C. J. 2001, *ApJL*, 553, L153, doi: [10.1086/320685](https://doi.org/10.1086/320685)

Herczeg, G. J., Wood, B. E., Linsky, J. L., Valenti, J. A., & Johns-Krull, C. M. 2004, *ApJ*, 607, 369, doi: [10.1086/383340](https://doi.org/10.1086/383340)

Hernández, J., Hartmann, L., Megeath, T., et al. 2007, *ApJ*, 662, 1067, doi: [10.1086/513735](https://doi.org/10.1086/513735)

Hollenbach, D., Johnstone, D., Lizano, S., & Shu, F. 1994, *ApJ*, 428, 654, doi: [10.1086/174276](https://doi.org/10.1086/174276)

Hollenbach, D., & McKee, C. F. 1989, *ApJ*, 342, 306, doi: [10.1086/167595](https://doi.org/10.1086/167595)

Hollenbach, D. J., Yorke, H. W., & Johnstone, D. 2000, in *Protostars and Planets IV*, ed. V. Mannings, A. P. Boss, & S. S. Russell, 401–428

Ingleby, L., Calvet, N., Hernández, J., et al. 2011, *AJ*, 141, 127, doi: [10.1088/0004-6256/141/4/127](https://doi.org/10.1088/0004-6256/141/4/127)

Johnston, K. G., Hoare, M. G., Beuther, H., et al. 2020, *ApJ*, 896, 35, doi: [10.3847/1538-4357/ab8adc](https://doi.org/10.3847/1538-4357/ab8adc)

Johnstone, D., Hollenbach, D., & Bally, J. 1998, *ApJ*, 499, 758, doi: [10.1086/305658](https://doi.org/10.1086/305658)

Kennedy, G. M., & Kenyon, S. J. 2009, *ApJ*, 695, 1210, doi: [10.1088/0004-637X/695/2/1210](https://doi.org/10.1088/0004-637X/695/2/1210)

Kuiper, R., Klahr, H., Dullemond, C., Kley, W., & Henning, T. 2010, *A&A*, 511, A81, doi: [10.1051/0004-6361/200912355](https://doi.org/10.1051/0004-6361/200912355)

Kuiper, R., & Klessen, R. S. 2013, *A&A*, 555, A7, doi: [10.1051/0004-6361/201321404](https://doi.org/10.1051/0004-6361/201321404)

Kunitomo, M., Suzuki, T. K., & Inutsuka, S.-i. 2020, *MNRAS*, 492, 3849, doi: [10.1093/mnras/staa087](https://doi.org/10.1093/mnras/staa087)

Lada, C. J., Muench, A. A., Luhman, K. L., et al. 2006, *AJ*, 131, 1574, doi: [10.1086/499808](https://doi.org/10.1086/499808)

Liffman, K. 2003, *PASA*, 20, 337, doi: [10.1071/AS03019](https://doi.org/10.1071/AS03019)

Lynden-Bell, D., & Pringle, J. E. 1974, *MNRAS*, 168, 603, doi: [10.1093/mnras/168.3.603](https://doi.org/10.1093/mnras/168.3.603)

Mamajek, E. E. 2009, in *American Institute of Physics Conference Series*, Vol. 1158, American Institute of Physics Conference Series, ed. T. Usuda, M. Tamura, & M. Ishii, 3–10, doi: [10.1063/1.3215910](https://doi.org/10.1063/1.3215910)

Mendigutía, I., Mora, A., Montesinos, B., et al. 2012, *A&A*, 543, A59, doi: [10.1051/0004-6361/201219110](https://doi.org/10.1051/0004-6361/201219110)

Meyer, M. R., Backman, D. E., Weinberger, A. J., & Wyatt, M. C. 2007, in *Protostars and Planets V*, ed. B. Reipurth, D. Jewitt, & K. Keil, 573.
<https://arxiv.org/abs/astro-ph/0606399>

Mignone, A., Bodo, G., Massaglia, S., et al. 2007, *ApJS*, 170, 228, doi: [10.1086/513316](https://doi.org/10.1086/513316)

Muzerolle, J., Hillenbrand, L., Calvet, N., Briceño, C., & Hartmann, L. 2003, *ApJ*, 592, 266, doi: [10.1086/375704](https://doi.org/10.1086/375704)

Najita, J. R., & Bergin, E. A. 2018, *ApJ*, 864, 168, doi: [10.3847/1538-4357/aad80c](https://doi.org/10.3847/1538-4357/aad80c)

Najita, J. R., Strom, S. E., & Muzerolle, J. 2007, *MNRAS*, 378, 369, doi: [10.1111/j.1365-2966.2007.11793.x](https://doi.org/10.1111/j.1365-2966.2007.11793.x)

Nakatani, R., Hosokawa, T., Yoshida, N., Nomura, H., & Kuiper, R. 2018a, *ApJ*, 857, 57, doi: [10.3847/1538-4357/aab70b](https://doi.org/10.3847/1538-4357/aab70b)

—. 2018b, *ApJ*, 865, 75, doi: [10.3847/1538-4357/aad9fd](https://doi.org/10.3847/1538-4357/aad9fd)

Nelson, R. P., & Langer, W. D. 1997, *ApJ*, 482, 796, doi: [10.1086/304167](https://doi.org/10.1086/304167)

Oliveira, I., Pontoppidan, K. M., Merín, B., et al. 2010, *ApJ*, 714, 778, doi: [10.1088/0004-637X/714/1/778](https://doi.org/10.1088/0004-637X/714/1/778)

Omukai, K., Hosokawa, T., & Yoshida, N. 2010, *ApJ*, 722, 1793, doi: [10.1088/0004-637X/722/2/1793](https://doi.org/10.1088/0004-637X/722/2/1793)

Osterbrock, D. E. 1989, *Astrophysics of gaseous nebulae and active galactic nuclei* (University Science Books)

Owen, J. E., Ercolano, B., Clarke, C. J., & Alexander, R. D. 2010, *MNRAS*, 401, 1415, doi: [10.1111/j.1365-2966.2009.15771.x](https://doi.org/10.1111/j.1365-2966.2009.15771.x)

Pascucci, I., Testi, L., Herczeg, G. J., et al. 2016, *ApJ*, 831, 125, doi: [10.3847/0004-637X/831/2/125](https://doi.org/10.3847/0004-637X/831/2/125)

Pollack, J. B., Hollenbach, D., Beckwith, S., et al. 1994, *ApJ*, 421, 615, doi: [10.1086/173677](https://doi.org/10.1086/173677)

Preibisch, T., Kim, Y.-C., Favata, F., et al. 2005, *ApJS*, 160, 401, doi: [10.1086/432891](https://doi.org/10.1086/432891)

Ribas, Á., Bouy, H., & Merín, B. 2015, *A&A*, 576, A52, doi: [10.1051/0004-6361/201424846](https://doi.org/10.1051/0004-6361/201424846)

Ribas, Á., Merín, B., Bouy, H., & Maud, L. T. 2014, *A&A*, 561, A54, doi: [10.1051/0004-6361/201322597](https://doi.org/10.1051/0004-6361/201322597)

Richling, S., & Yorke, H. W. 2000, *ApJ*, 539, 258, doi: [10.1086/309198](https://doi.org/10.1086/309198)

Santoro, F., & Shull, J. M. 2006, *ApJ*, 643, 26, doi: [10.1086/501518](https://doi.org/10.1086/501518)

Schindhelm, E., France, K., Herczeg, G. J., et al. 2012, *ApJL*, 756, L23, doi: [10.1088/2041-8205/756/1/L23](https://doi.org/10.1088/2041-8205/756/1/L23)

Shakura, N. I., & Sunyaev, R. A. 1973, *A&A*, 500, 33

Shu, F., Najita, J., Ostriker, E., et al. 1994, *ApJ*, 429, 781, doi: [10.1086/174363](https://doi.org/10.1086/174363)

Siebenmorgen, R., & Krügel, E. 2010, *A&A*, 511, A6, doi: [10.1051/0004-6361/200912035](https://doi.org/10.1051/0004-6361/200912035)

Spitzer, L. 1978, Physical processes in the interstellar medium (Wiley-Interscience), doi: [10.1002/9783527617722](https://doi.org/10.1002/9783527617722)

Störzer, H., & Hollenbach, D. 1999, *ApJ*, 515, 669, doi: [10.1086/307055](https://doi.org/10.1086/307055)

Suzuki, T. K., & Inutsuka, S.-i. 2009, *ApJL*, 691, L49, doi: [10.1088/0004-637X/691/1/L49](https://doi.org/10.1088/0004-637X/691/1/L49)

Suzuki, T. K., Ogiara, M., Morbidelli, A. r., Crida, A., & Guillot, T. 2016, *A&A*, 596, A74, doi: [10.1051/0004-6361/201628955](https://doi.org/10.1051/0004-6361/201628955)

Tanaka, K. E. I., Nakamoto, T., & Omukai, K. 2013, *ApJ*, 773, 155, doi: [10.1088/0004-637X/773/2/155](https://doi.org/10.1088/0004-637X/773/2/155)

Turner, N. J., Fromang, S., Gammie, C., et al. 2014, in *Protostars and Planets VI*, ed. H. Beuther, R. S. Klessen, C. P. Dullemond, & T. Henning, 411, doi: [10.2458/azu_uapress_9780816531240-ch018](https://doi.org/10.2458/azu_uapress_9780816531240-ch018)

Vicente, S., Berné, O., Tielens, A. G. G. M., et al. 2013, *ApJL*, 765, L38, doi: [10.1088/2041-8205/765/2/L38](https://doi.org/10.1088/2041-8205/765/2/L38)

Vidotto, A. A., Gregory, S. G., Jardine, M., et al. 2014, *MNRAS*, 441, 2361, doi: [10.1093/mnras/stu728](https://doi.org/10.1093/mnras/stu728)

Wang, L., Bai, X.-N., & Goodman, J. 2019, *ApJ*, 874, 90, doi: [10.3847/1538-4357/ab06fd](https://doi.org/10.3847/1538-4357/ab06fd)

Wang, L., & Goodman, J. 2017, *ApJ*, 847, 11, doi: [10.3847/1538-4357/aa8726](https://doi.org/10.3847/1538-4357/aa8726)

Williams, J. P., & Andrews, S. M. 2005, arXiv e-prints, astro. <https://arxiv.org/abs/astro-ph/0511589>

Wölfer, L., Picogna, G., Ercolano, B., & van Dishoeck, E. F. 2019, *MNRAS*, 490, 5596, doi: [10.1093/mnras/stz2939](https://doi.org/10.1093/mnras/stz2939)

Yang, H., Herczeg, G. J., Linsky, J. L., et al. 2012, *ApJ*, 744, 121, doi: [10.1088/0004-637X/744/2/121](https://doi.org/10.1088/0004-637X/744/2/121)

Yasui, C., Kobayashi, N., Tokunaga, A. T., & Saito, M. 2014, *MNRAS*, 442, 2543, doi: [10.1093/mnras/stu1013](https://doi.org/10.1093/mnras/stu1013)

Yorke, H. W., & Welz, A. 1996, *A&A*, 315, 555